Influence of Liquid Film Characteristics on Hot Cracking Initiation in Al–Cu Alloys at the End of Solidification

Ming Su[1] · Xiaoguang Yuan[1] · Chunyu Yue[1] · Wentao Zheng[1] · Yuxiang Wang[1] · Jian Kang[1]

Abstract

In this study, Al–4Cu alloy specimens with spherical grains and liquid films were obtained by isothermal reheating treatment. The hot cracking of the solidification process was determined using a modified constrained rod casting experimental apparatus, and the effect of liquid film characteristics at the end of solidification on hot cracking initiation of Al–4Cu alloys was systematically investigated by combining molecular dynamics simulations and other methods. With the extension of soaking time, the liquid fraction (liquid film fraction at the end of solidification) and grain shape factor increased with higher isothermal reheating temperatures. Additionally, the widened filling channel decreased the hot cracking initiation temperature and the critical hot cracking shrinkage stress was found to increase, thus reducing the hot cracking severity in Al–4Cu alloys. Molecular dynamics simulations revealed that with the extension of soaking time, the composition of the liquid film changed at different isothermal reheating temperatures, but the short-range structure and atomic ordering of the liquid film remained the same. The activity of the liquid film increased in equilibrium, leading to a decrease in viscosity and an increase in fluidity, which contributed to the filling behaviour. After isothermal reheating at 640 °C for 60 min, the liquid fraction reached the maximum, and the viscosity of the liquid film was the minimum. In addition, almost no hot cracks were found.

Keywords Al–4Cu alloy · Liquid film characteristics · Isothermal reheating · Molecular dynamics simulation · Hot cracking initiation mechanism

1 Introduction

Al–Cu alloys have been widely used in many fields such as the aerospace industry, automobile industry and mechanical equipment, because of their low density, high specific strength and strong corrosion resistance [1, 2]. Despite their advantages, the limiting factor of Al–Cu alloys is their high susceptibility to various defects in castings, such as shrinkage porosity, hot cracking, segregation and microporosity, due to their wide solidification temperature range and large solidification shrinkage [3, 4]. These defects are more serious in thin-walled castings, which restricts the wide application of Al–Cu alloys [5, 6].

Hot cracking is the most common and serious defect in Al–Cu alloys at the end of solidification, which leads to a drastic reduction in the mechanical properties of the castings [7]. To reduce hot cracking and determine the mechanism of hot cracking initiation in Al–Cu alloys, a series of studies have been performed by many researchers. D' Elia et al. [8] investigated the influencing factors of the hot cracking severity in cast Al–Cu alloys using constrained rod casting (CRC) experiments and found that refining the grain and increasing the mould temperature could increase the fluidity of the liquid film at the end of solidification and extend the filling time, thus effectively reducing the hot cracking. D' Elia et al. [9] also investigated the mechanism of liquid film feeding in a B206 Al–Cu alloy. Their results revealed that the eutectic phase rich liquid film did not fill the hot cracks completely at the end of solidification. Yang et al. [10] reported that the addition of TiC particles refined the grain size of Al–Cu alloys and improved the hot cracking resistance of Al–Cu alloys. Li et al. [3] reported that the hot cracking severity of

✉ Xiaoguang Yuan
   yuanxg@sut.edu.cn

✉ Wentao Zheng
   wenntaozheng@163.com

1 School of Materials Science and Engineering, Shenyang University of Technology, Shenyang 110870, China

Al–Cu alloy castings decreased with increasing wall thickness using CRC experiments, while grain refinement was found to reduce the shrinkage of the liquid phase between the dendrites. Shabestari et al. [11] reported that hot cracks in Al–Cu alloys always formed in the mushy zone at the end of solidification by thermal analysis. Due to the variation in mushy zone properties for different cooling rates, the resistance to hot cracking was improved. Liu and Kou [12] reviewed that hot cracks occurred at the end of solidification. Thus, Liu and Kou [13] also revealed that hot cracks usually emerged in grain boundaries as a consequence of fewer liquid films between grain boundaries. Collectively, the studies presented thus far provide evidence that hot cracks occurred at the residual liquid phase and extended along the grain boundaries in the final stage of solidification [14], which was due to insufficient liquid film fluidity to resist solidification shrinkage at the end of solidification [15, 16]. Therefore, the liquid film is an important component in reducing hot cracks in the alloy and plays a key role in restraining the shrinkage of the alloy.

Early research on hot cracking initiation suggested that hot cracks resulted from local thermal stress concentrations [17, 18]. Therefore, Takai et al. [19] determined that the grain refined structure elongation was greater than that in the coarse grain structure regardless of the solid fraction. Furthermore, Takai et al. [20] determined the relationship between hot cracking initiation and the magnitude of tensile force by applying an active load to the mushy zone at the end of solidification and collected images by high-speed photography based on a CRC experiment. Matsushita et al. [21] established a solid–liquid two-phase finite element model with a liquid film skeleton structure based on the water-quenched organization of the casting at the end of solidification and determined the critical stress to separate the liquid and solid phases by finite element simulations. Xu et al. [22, 23] found that the liquid film of the Al–Si alloy was elongated and was able to resist tensile force under active loading tension and built a hot cracking criterion model based on the nominal yield stress. The current research on the liquid film and the mushy zone at the end of solidification was limited to active loading tension to determine the constitutive model and the hot cracking severity. However, the shrinkage force during solidification was extremely complicated, and the active loading tension could not be used on behalf of the shrinkage force.

The liquid film characteristics play a crucial role in hot cracking during the solidification process. The liquid film characteristics include the structural characteristics, radial distribution function (RDF), diffusivity coefficient (D) and viscosity (η) [24, 25]. The liquid film characteristics change with the solidification process and are difficult to characterize by experimental methods. Due to the rapid development of the computational material sciences, theoretical studies of the atomic structure evolution upon solidification from the metallic liquid have become possible. Factors that influence metallic liquid characteristics have been explored in several studies. Roik et al. [26] calculated the RDF of binary Al alloys by molecular dynamics (MD) simulation and found that the melting binary Al alloys had a short-range structure, and different melting binary Al alloy structures led to differences in their characteristics. Wang et al. [27] calculated the local structure, D and η of liquid binary Al–xZr alloys by MD simulation, and demonstrated that different contents of Zr could affect the characteristics of liquid Al–xZr alloys. Therefore, MD simulation is a reliable method to confirm the characteristics of metallic liquids and provides theoretical support for this study to calculate the characteristics of liquid films.

As previously stated, the CRC experiment is a valid and widely used method to determine the hot cracking severity in casting alloys [28, 29]. In this research, a modified constrained rod casting (MCRC) experimental apparatus equipped with a load cell was developed to determine the onset temperature of hot cracks. The isothermal remelting treatment of nondendritic structure Al–4Cu alloy specimens was used to reproduce the intergranular liquid film skeleton structure, and the solidification shrinkage force under different isothermal remelting conditions was measured to establish the relationship between the critical cracking stress and the liquid fraction. The influence mechanism of liquid films on hot crack initiation was investigated by observing the morphology of hot cracks. MD simulation was used to quantify the characteristics of the liquid film and verify the effect of liquid film characteristics on hot crack initiation.

2 Experimental

2.1 Materials

Al–4Cu alloys with a high hot cracking severity were used in this study. Al–4Cu billets with nondendritic structures were fabricated by mechanical stirring. First, high-purity Al was placed in a crucible that was preheated to 500 °C and subsequently heated to 750 °C. Al–50Cu was added to the high-purity Al melt. Until the alloy was completely melted, the refining agent, deslagging agent and deoxidizer (C_2Cl_6) were added in order and held for 10 min (the amount of each addition was 0.5–0.7 wt% of the molten metal). Finally, the alloy melt was poured into the H13 steel mould which was coated with a zinc oxide solution in the cavity and preheated to 300 °C. The microstructure was observed by optical microscopy (OM, ZEISS). The phase composition was determined by an X-ray diffractometer (XRD, SHIMADZU XRD-7000) equipped with a Cu $K\alpha$ source radiation and a transmission electron microscope (TEM, JEM-2100). XRD patterns were

recorded in the 2θ range of 20°–100° at a scan speed of 2°/min. TEM analysis was conducted at 200 kV. The thin foil specimen for TEM analysis was ground to 50 μm thickness, and then, a 3-mm disc was punched out before ion milling.

2.2 Isothermal Remelting Treatment

A DSC-S1000 differential scanning calorimeter (DSC) apparatus was used to determine the range of isothermal remelting temperatures. The samples were heated to 700 °C at 10 °C min^{-1} under a nitrogen atmosphere. As indicated in Fig. 1, based on the DSC curve, the solidus and liquidus temperatures of Al–4Cu alloys were 549 °C and 663 °C, respectively. The liquid fraction versus the temperature curve was obtained by integrating the DSC curve. Considering that the DSC heating rate was close to the actual isothermal reheating rate, the theoretical liquid fraction versus temperature curve of the Al–4Cu alloy specimens measured in DSC was used as a reference for determining the isothermal remelting experimental temperature [30].

The isothermal remelting experiment was performed using a tubular resistance furnace (1 kW, 220 V) to heat a cylindrical specimen with a diameter of 6 mm and a length of 30 mm (surface pretreatment of the specimens prior to microstructure observation). The oxide film formed during the heating process had no effect on the experimental results, and thus, protective gas was not required. As shown in Fig. 1, isothermal reheating temperatures of 620 °C, 630 °C and 640 °C, corresponding to theoretical liquid fractions of 10%, 15% and 25%, respectively, were determined from the DSC curves. The samples were soaked for 10 min, 20 min, 30 min, 40 min, 50 min and 60 min at each given temperature and then quickly quenched in cold water to preserve the microstructure obtained at the isothermal remelting stage. OM was used
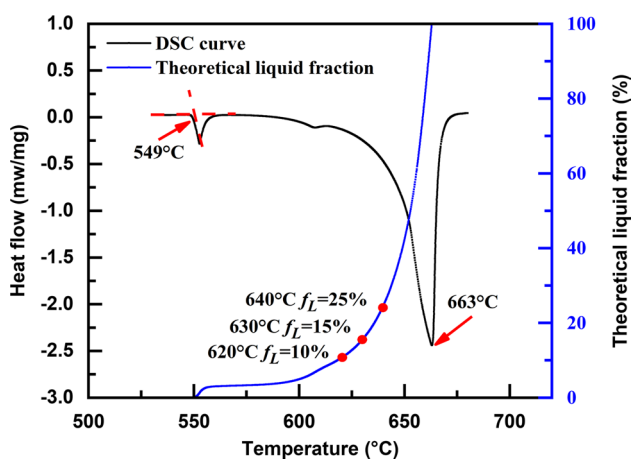
to observe the microstructure after water quenching. The elemental distribution of the semisolid microstructure after water quenching was analysed by electron probe microanalysis (EPMA, EPMA-1720). In this study, the experimental liquid fraction (LF) and shape factor (SF) of solid grains were measured by Image-Pro Plus 6.0 software. LF and SF were defined using Eqs. (1) and (2), respectively [31, 32].

$$LF = \frac{A_L}{A_{Total}} \times 100\% \tag{1}$$

$$SF = \frac{\sum_{i=1}^{N} 4\pi A_i / P_i^2}{N} \tag{2}$$

where A_L, A_{Total}, A_i, P_i and N are the area of the liquid, area of the micrograph area, area of the solid grains, perimeter of the solid grains and total number of solid grains, respectively.

2.3 Liquid Film Shrinkage Stress Test Device

In this study, the shrinkage stress of the liquid film at the end of solidification was measured by an MCRC apparatus, as shown in Fig. 2a. The Al–4Cu alloy specimens with spherical solid and liquid films were obtained by isothermal reheating treatment in a tube resistance furnace. First, the temperature of the tube resistance furnace was increased to the set value and was kept for 30 min to make the interior temperature of the tube furnace uniform and stable. Then, one end of the specimen was held by a restraining rod, and the other end was connected to a connecting rod. The tube furnace was turned off after the scheduled holding time, and the stress sensor was connected to the connecting rod so that it collected the contraction stress of the liquid film during solidification and cooling. The data acquisition system included the thermocouple, the stress sensor and the computer data acquisition device. The real-time data measured by the thermocouple and the stress sensor were stored on the computer through the data acquisition system, as illustrated in Fig. 2b. The diameter of the specimen used to measure the shrinkage stress of the liquid film at the end of solidification was the same as that in the isothermal remelting experiment to ensure that the microstructure morphology of both was the same, and the specimen size is shown in Fig. 2c. Microstructure observation and compositional analysis of hot cracks after solidification were performed by a scanning electron microscope (SEM, HITACHI-S3400 N) equipped with an energy-dispersive spectrometer (EDS) operating at 20 kV.
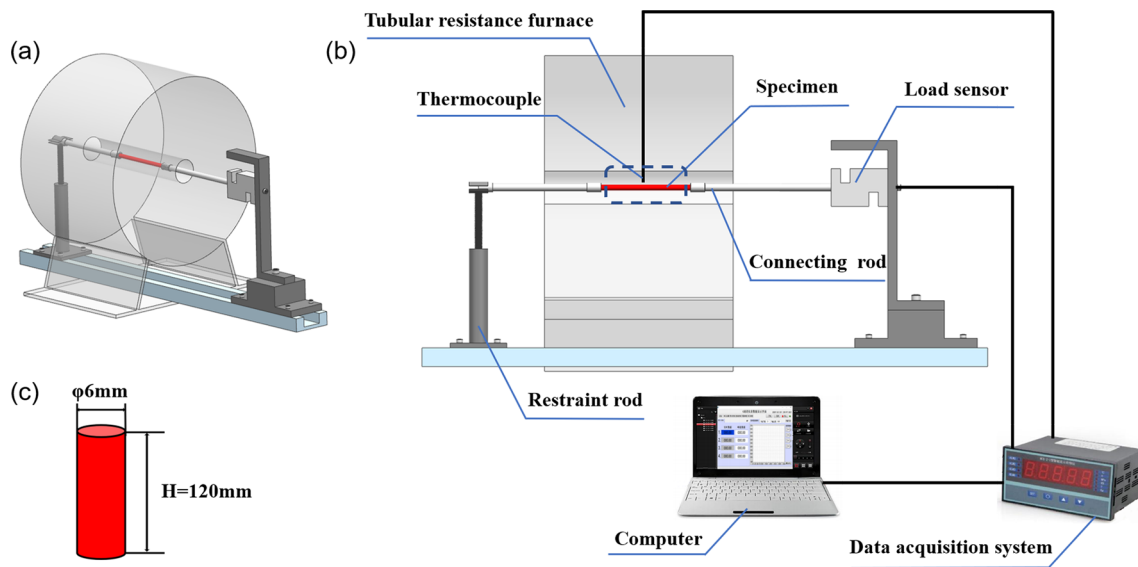

Fig. 1 DSC curve and theoretical liquid fraction versus temperature of the Al–4Cu alloy

Fig. 2 Schematic diagram of the experimental system for liquid film shrinkage stress: **a** isothermal reheating treatment experiment device, **b** overall experimental system and **c** size of the specimen

2.4 MD Simulation

In this study, RDF, D and η were used to characterize the liquid film. D was derived from Einstein's relation [33] through the mean square displacement (MSD) as a function of time, as shown in Eq. (3),

$$D = \lim_{t \to \infty} \frac{\left\langle R^2(t) \right\rangle}{6t} \tag{3}$$

where t is time and $<R^2(t)>$ is the MSD as a function of time. RDF and D are obtained from MD simulation, and η of liquid films at different isothermal remelting conditions can be derived from the Stokes–Einstein equation as follows [34]:

$$\eta = \frac{kT}{2\pi aD} \tag{4}$$

where the parameters of k, T and D are Boltzmann's constant, temperature and diffusion coefficient, respectively. The parameter a denotes the effective atomic diameter, which can be determined by the position of the first peak in the RDF.

The MD simulation of the liquid film in this work was conducted by Material Studio (version 2019) software using the Focite package based on potential function theory. A cubic $5 \times 5 \times 5$ supercell with periodic boundary conditions was built, where the atoms were randomly distributed in the initial state. The simulations were calculated by the canonical NVT ensemble (fixed atom number, volume and temperature). The temperature was controlled by the velocity scaling method. At each isothermal remelting condition, the

liquid film system reached an equilibrium state of 200 ps, and the evolution of the atomic structure is presented in Fig. 3.

3 Results

3.1 Microstructure Evolution of Al–4Cu Alloys During Isothermal Remelting Treatment

The microstructure of the Al–4Cu alloy billets is presented in Fig. 4a. It can be found that the grains had a nondendritic morphology and the eutectic phase was distributed at the grain boundaries. The phase composition of the Al–4Cu alloy billets was initially determined to be α-Al and Al$_2$Cu by XRD, as indicated in Fig. 4b. The eutectic phase distributed at the grain boundaries was identified to be Al$_2$Cu with a striped shape by TEM, as shown in Fig. 4c.

The EPMA mapping of the main alloying elements of Al–4Cu alloy billets after isothermal reheating treatment at 630 °C for 50 min is presented in Fig. 5. The lighter colour of the elemental intensity scale means a greater concentration of elements and a higher elemental content at this location. The solid grains and liquid phases at the grain boundaries are observed in Fig. 5a. As shown in Fig. 5b, c, Al and Cu elements in the liquid phase were distributed between the grain boundaries, and only a few Cu elements distributed within the α-Al solid grains.

The effects of the isothermal remelting treatment temperature and time on the semisolid microstructure of Al–4Cu alloys are illustrated in Fig. 6. Figure 6a–c shows the
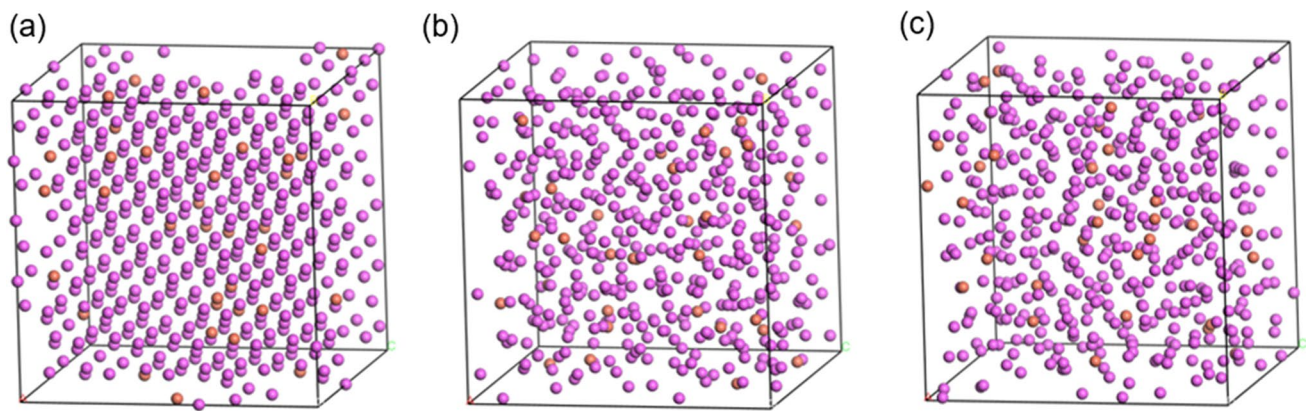
Fig. 3 Atomic structure evolution of liquid films after isothermal reheating treatment at 630 °C for 50 min: **a** 0 ps, **b** 100 ps, **c** 200 ps
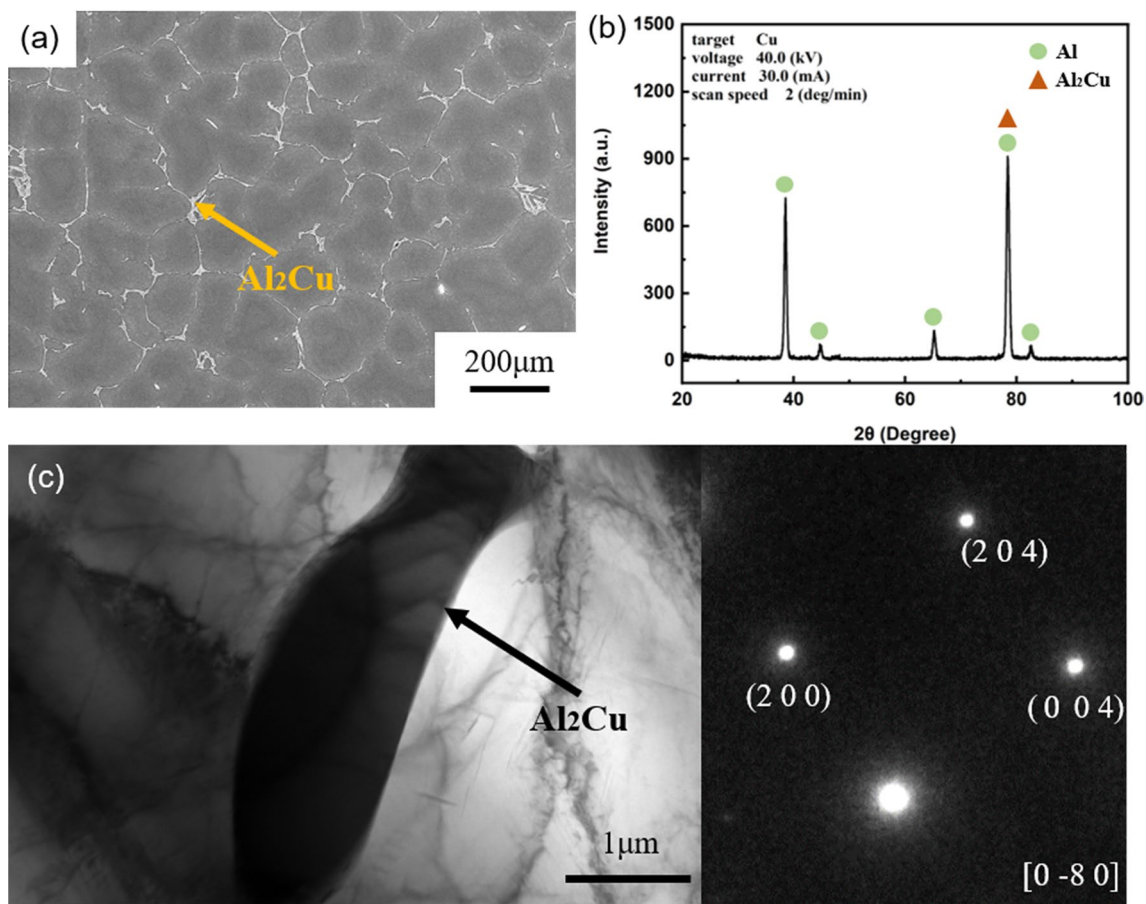

Fig. 4 Microstructures and phase composition of the billet of Al–4Cu alloy: **a** OM, **b** XRD, **c** TEM

microstructures of Al–4Cu alloys after isothermal remelting treatment at 620 °C for different soaking time. As shown in Fig. 6a, the eutectic phase Al$_2$Cu at the grain boundaries was completely melted to form liquid films with skeleton network channels and surrounding the solid grains after isothermal remelting treatment at 620 °C for 20 min. The

small α-Al solid grains had a higher spheroidization degree, while the large ones had different sizes and shapes, and the grain edges were irregular. The lower spherization degree of α-Al solid grains was caused by few liquid films at the grain boundaries after short-time soaking. The increase in liquid film thickness and the form of interconnected liquid
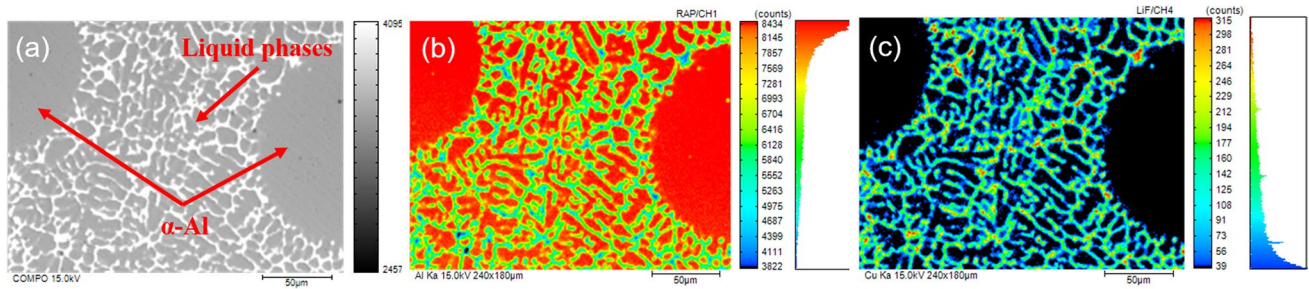
Fig. 5 EPMA analysis mapping results of Al–Cu alloys after isothermal reheating treatment at 630 °C for 50 min: **a** OM, **b** Al and **c** Cu
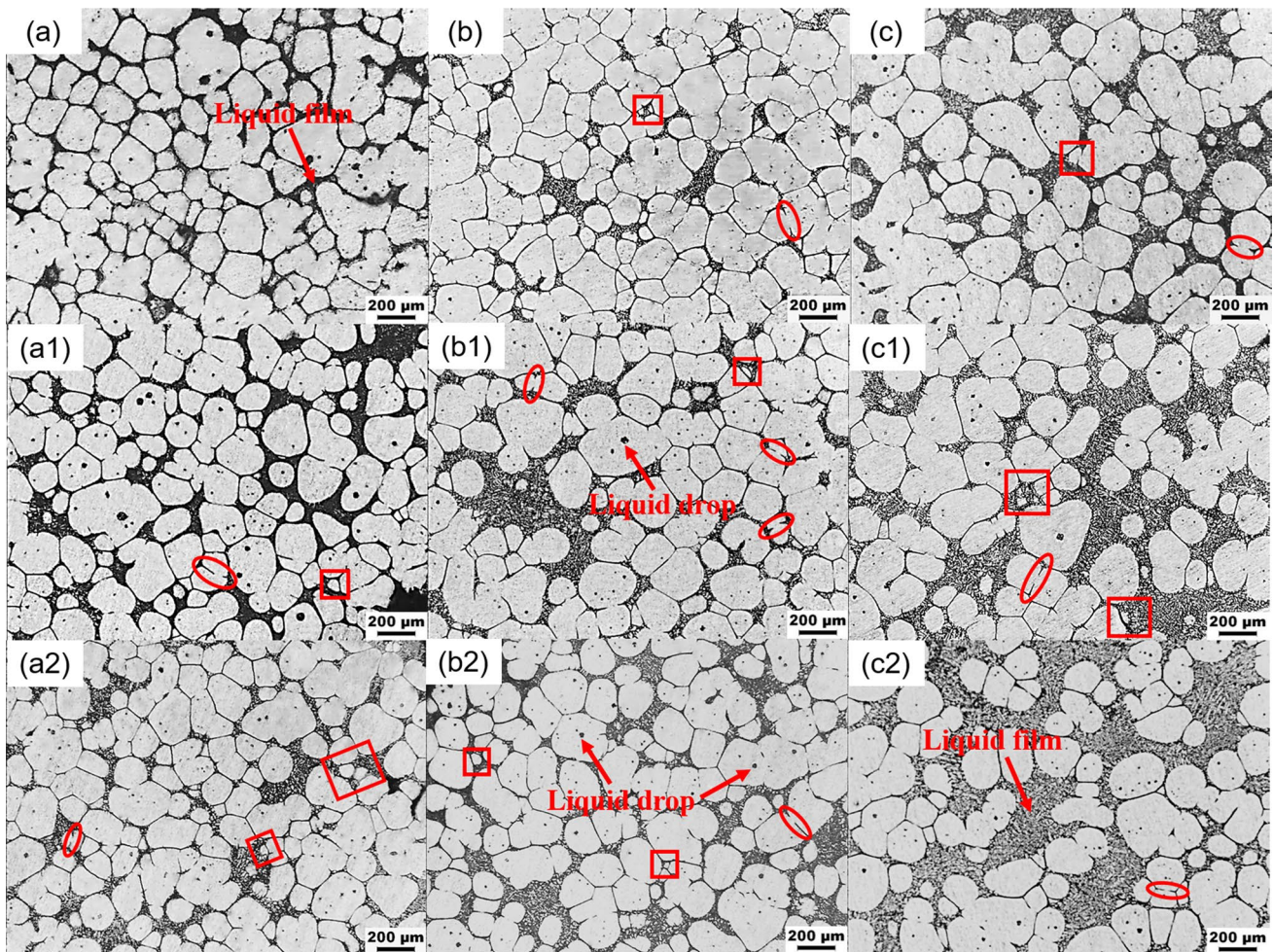

Fig. 6 Microstructures of Al–4Cu alloys after isothermal reheating treatment: **a** 620 ℃, 20 min; **b** 620 ℃, 40 min; **c** 620 ℃, 60 min; **a1** 630 ℃, 20 min; **b1** 630 ℃, 40 min; **c1** 630 ℃, 60 min; **a2** 640 ℃, 20 min; **b2** 640 ℃, 40 min; **c2** 640 ℃, 60 min

film skeleton network channels were associated with the increased soaking time, while the spherization degree and grain sizes of α-Al solid grains gradually increased, as illustrated in Fig. 6b, c. The reason for the above-mentioned phenomenon was, on the one hand, Ostwald ripening (see the red boxes) which was noticed that the increase in soaking time enhanced the growth of the large grains and the small grains were observed to melt. On the other hand, the thin liquid film reduced the distance between grains, and different solid grains with the same crystal orientation coalesced together (see the red ellipses), which was consistent with the results of Jiang et al. [35].

Figure 6a1, b1 and c1 presents the microstructures of Al–4Cu alloys after isothermal remelting treatment at 630 °C for different soaking time. As can be seen in Fig. 6a1, the eutectic phase Al$_2$Cu was completely melted and formed interconnected liquid films with skeleton network channels, and Ostwald ripening and coalescence growth were observed. In addition, at 630 °C for 20 min, the spheroidization degree of α-Al solid grains increased compared to that at 620 °C for 20 min. Some large intragranular liquid drops that broke the original grain boundaries occurred within α-Al solid grains, as presented by the red arrows in Fig. 6b1. These liquid drops gradually decreased and even disappeared with the extension of soaking time, which was caused by the movement of intragranular liquid drops to the grain boundaries or the migration of the liquid film along the grain boundaries [36]. The interconnected liquid film skeleton network channel thickness peaked after 60 min of soaking.

Figure 6a2, b2 and c2 indicates the microstructures of the Al–4Cu alloy after isothermal remelting treatment at 640 °C for different soaking time. A similar microstructure evolution can be obtained compared to that at 630 °C and 640 °C. In contrast, as presented in Fig. 6c2, the liquid drops within the α-Al solid grains significantly reduced, and the skeleton network channels of the liquid films became wider. At the same time, the spheroidization of α-Al solid grains increased, and most grains were spherical and rounded rod-shaped.

The variations in SF and LF with isothermal treatment time at different temperatures are presented in Fig. 7 using Eqs. (1) and (2). As shown in Fig. 7a, the SF always remained between 0.7 and 0.85 under different isothermal remelting treatment conditions, and the SF slightly increased

with increasing isothermal remelting treatment temperature and soaking time, which was mainly due to Ostwald ripening. The SF value reached a maximum value of 0.822 after isothermal remelting treatment at 640 °C for 60 min. As shown in Fig. 7b, the increased LF and wider liquid film network channels were associated with the increased isothermal remelting treatment temperature and soaking time. The LF significantly increased and the LF value reached a maximum value of 36.68% after isothermal remelting treatment at 640 °C for 60 min.

3.2 Stress–Temperature–Time Curves

To ensure the accuracy of the experimental results, the MCRC apparatus was designed to minimize the effect of the restraining rod and connecting rod on the measured shrinkage force. On the one hand, the tube resistance furnace was designed with a short heating zone, a holding temperature zone and a transition zone. The connecting rod and restraining rod were completely exposed outside the tube resistance furnace for convective heat exchange with the air. The tube resistance furnace did not heat the connecting rod and restraining rod directly. The increased temperature of the connecting rod and restraining rod was caused by heat transfer from the Al–4Cu alloy specimens. As a result, the temperature increase of the restraining rod and connecting rod was effectively reduced. On the other hand, the connecting rod and restraining rod were made of 304 stainless steel. The thermal conductivities of 304 stainless steel and Al–Cu alloy are 12.47 W/(m K) [37] and 197 W/(m K) [38], respectively. The thermal conductivity of 304 stainless steel is much smaller than that of the Al–Cu alloy. Therefore, the temperature of the connecting rod and restraining rod
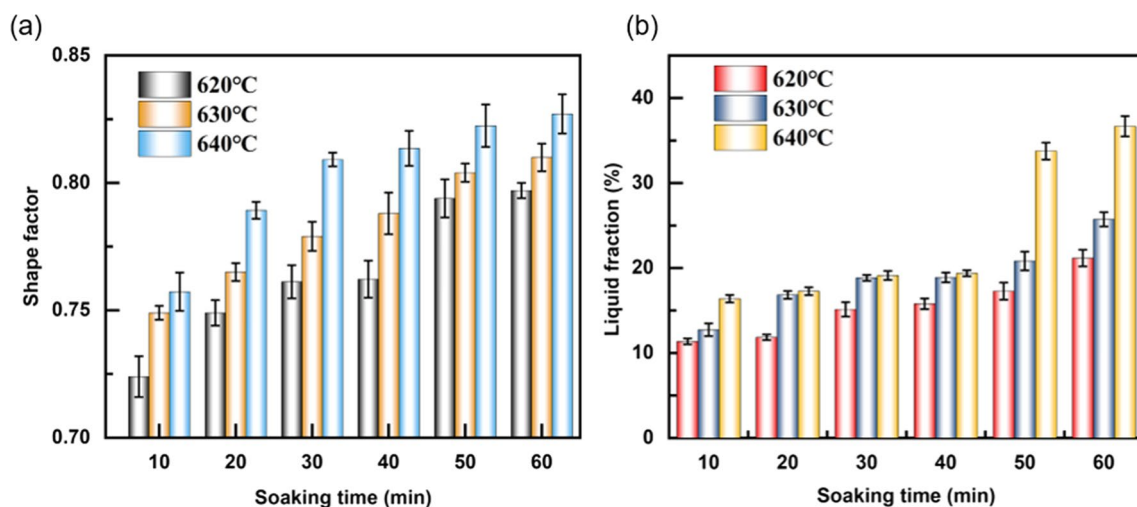

Fig. 7 Variation in the **a** average shape factor, **b** liquid fraction of Al–4Cu alloys at different temperatures for different isothermal reheating treatment time

slightly increased during the experiment. Meanwhile, the temperature of the connecting rod and restraining rod ranged from 80 to 120 ℃ during the pre-experiment for different isothermal remelting conditions. Therefore, the increased temperature of the connecting rod and restraining rod had negligible effects on the experimental results.

The stress–time and temperature–time curves for each isothermal reheating treatment condition are presented in Fig. 8. In this study, the cooling rate obtained from the temperature–time curves was approximately 0.1 °C/s. As the solidification commenced in the Al–4Cu alloy with near-spheroidal grains, both the liquid film and α-Al solid grains began to shrink, and the shrinkage of the liquid film played a major role in the entire solidification process, as reported by Zhou et al. [39] and Hao et al. [40]. Zhong et al. [41] and Du et al. [42] investigated the relationship between the stress–time curves and initiated hot cracks. Their results revealed that once stress release occurred on the stress–time curves, it indicated that hot cracks initiated on the specimen. Therefore, the critical hot cracking initiation shrinkage stress value of the liquid film and the corresponding critical hot cracking initiation temperature were obtained from the stress–temperature–time curves at each isothermal reheating treatment condition.

The stress–time and temperature–time curves for the 620 °C isothermal remelting treatment are illustrated in Fig. 8a–c, where the shrinkage stress of the liquid film gradually increased with the progress of solidification. Stress releases were observed at each isothermal reheating treatment time at 620 °C, indicating that hot cracks occurred in all cases. A gradual decrease in the
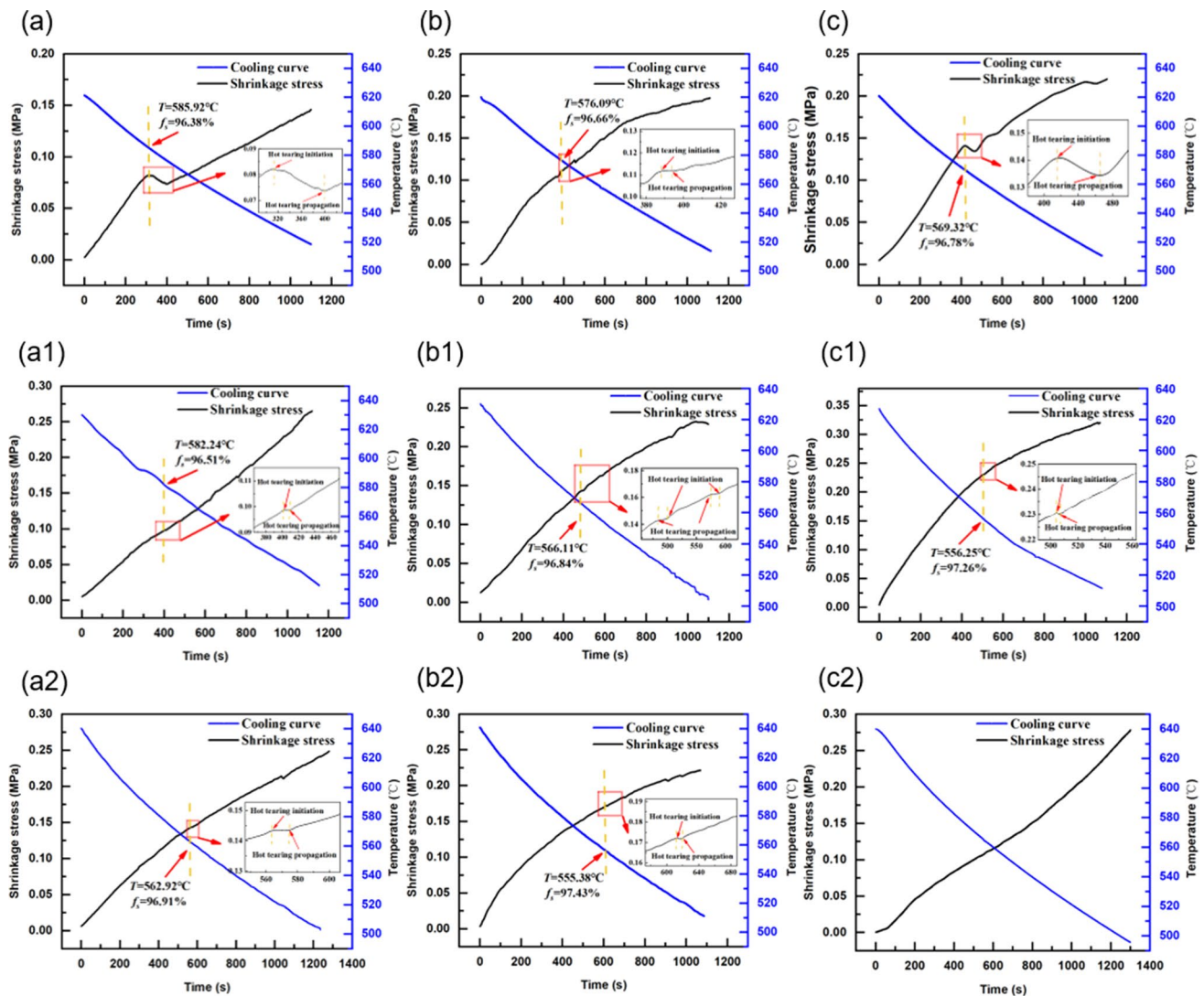

Fig. 8 Stress–temperature–time curves after isothermal treatment: **a** 620 ℃, 20 min; **b** 620 ℃, 40 min; **c** 620 ℃, 60 min; **a1** 630 ℃, 20 min; **b1** 630 ℃, 40 min; **c1** 630 ℃, 60 min; **a2** 640 ℃, 20 min; **b2** 640 ℃, 40 min; **c2** 640 ℃, 60 min

temperature of hot cracking initiation was evident for higher soaking time; in contrast, the shrinkage stress increased.

The stress–time and temperature–time curves for the 630 °C isothermal remelting treatment are displayed in Fig. 8a1, b1 and c1. Similar to 620 °C, stress release was also observed at each isothermal reheating treatment time, confirming that hot cracking occurred at 630 °C. Two successive stress releases occurred in the stress–time curves, as shown in Fig. 8b1, implying that crack propagation or secondary hot cracks occurred in the specimen due to the insufficient feeding capacity of the liquid film. Compared with the isothermal remelting temperature of 620 °C, the hot cracking initiation temperature decreased, while the liquid film shrinkage stress increased.

The stress–time and temperature–time curves for the 640 °C isothermal remelting treatment are displayed in Fig. 8a2, b2 and c2. The hot cracking initiation temperature significantly decreased, while the liquid film shrinkage stress increased compared to the isothermal reheating temperatures of 630 °C and 620 °C, as shown in Fig. 8a2, b2 and c2. In addition, no stress release was visible on the stress–time curve, indicating that almost no hot cracks occurred at the isothermal reheating temperature of 640 °C for 60 min.

Figure 9 lists the temperatures and liquid film shrinkage stresses when hot cracking initiated for each isothermal remelting condition. As can be seen from Fig. 9a, the hot cracking initiation temperature significantly decreased with higher isothermal remelting treatment temperatures and longer soaking time. The hot cracking initiation temperature at 640 °C for 50 min isothermal remelting treatment was 549.84 °C, which was very close to the solidus temperature, indicating that the hot crack was not prone to form under this condition. The curve illustrates a significant increase in

liquid film shrinkage stress with higher isothermal remelting treatment temperature and longer soaking time when hot cracking initiate, as presented in Fig. 9b.

Combined with Fig. 7, the preliminary analysis of the results in Fig. 9 is as follows. On the one hand, the difference in the feeding ability of liquid films was likely attributed to the varied composition and characteristics of the liquid film at each isothermal reheating treatment condition. On the other hand, with a higher isothermal remelting treatment temperature, the increased grain roundness after a longer soaking time created a wider feeding channel associated with a larger volume fraction of liquid films, which facilitated feeding, thus making the decrease in hot cracking initiation temperature. The liquid film characteristics were quantitatively calculated, and the mechanism of hot cracking initiation is discussed in detail in Sect. 4.

3.3 Hot Cracking Morphology Analysis

The solid fractions when hot cracking initiated in each isothermal remelting condition were measured according to Fig. 8, as listed in Table 1. The range of the solid fraction for hot cracking initiation was 95.87–99.60%. The Clyne–Davies theoretical model suggested that the solid grains formed a skeleton structure when the solid fraction was between 0.9 and 0.99. The reason for this phenomenon was revealed by D 'Elia et al. [43]. Their research illustrated that the closed skeleton structure impeded liquid film feeding, which easily caused intergranular hot cracking due to inadequate feeding. The range of the solid fraction for hot cracking initiation was smaller than that of the Clyne–Davies theoretical model, which was caused by the spherical solid grains during solidification in the present experiment. Combined with Fig. 1, no hot cracks commenced on specimens
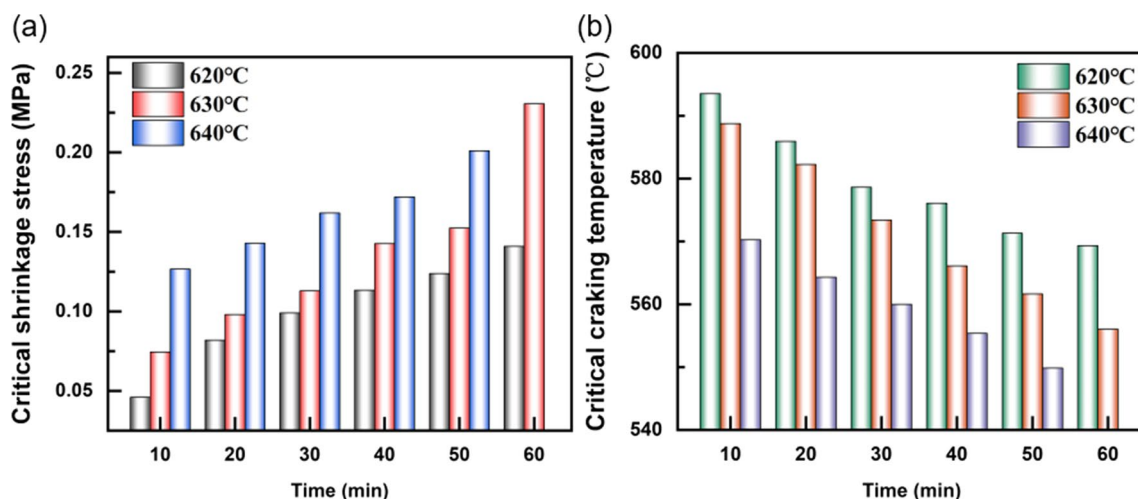

Fig. 9 Variations in **a** the critical temperature, **b** critical shrinkage stress of the liquid film of hot cracking initiation vs. isothermal treatment temperature and time

Table 1 Critical solid fraction (%) after hot cracking initiation for different isothermal treatment conditions

Time (min)	10	20	30	40	50	60
620	95.87	96.38	96.60	96.66	96.73	96.78
630	96.33	96.51	96.70	96.84	96.95	97.26
640	96.76	96.91	96.95	97.43	99.60	–

until eutectic Al_2Cu nucleated. As a result, the shrinkage of the specimen could only be accommodated mainly by feeding with eutectic-rich liquid as the last liquid available for feeding. Figure 10 shows the hot cracking morphology and EDS analysis. An increase in Cu elements and a decrease in Al elements were observed at the boundary of the hot crack (points A and B), as shown in Fig. 10a. This was attributed to the fact that the liquid film consisted of Al and Cu elements at the beginning of solidification, and the Al elements nucleated along the α-Al solid grains of the semisolid alloy as solidification progressed. The eutectic Al_2Cu nucleated on the grain boundary where hot cracks occurred at the last stage of solidification. The EDS results of the alloys at the end of feeding, presented in Fig. 10b, show that the ratio of Al to Cu atoms was almost 2:1. This further verified the eutectic Al_2Cu, implying that eutectic-rich liquid films attempted to fill and subsequently heal the developing cracks. However, the eutectic-rich liquid film was not successful at completely healing the hot cracks investigated in this research.

The hot cracking morphology after isothermal remelting for six soaking time at 630 °C is shown in Fig. 11. The morphology was characterized by hot cracks initiating through intergranular regions between two near α-Al grains with the eutectic phase Al_2Cu dispersed along or surrounding the propagation path. Crack propagation ended at the bridge between two solid α-Al grains or the eutectic phase Al_2Cu with sheet structure, as shown in Fig. 11a–d. The reason was
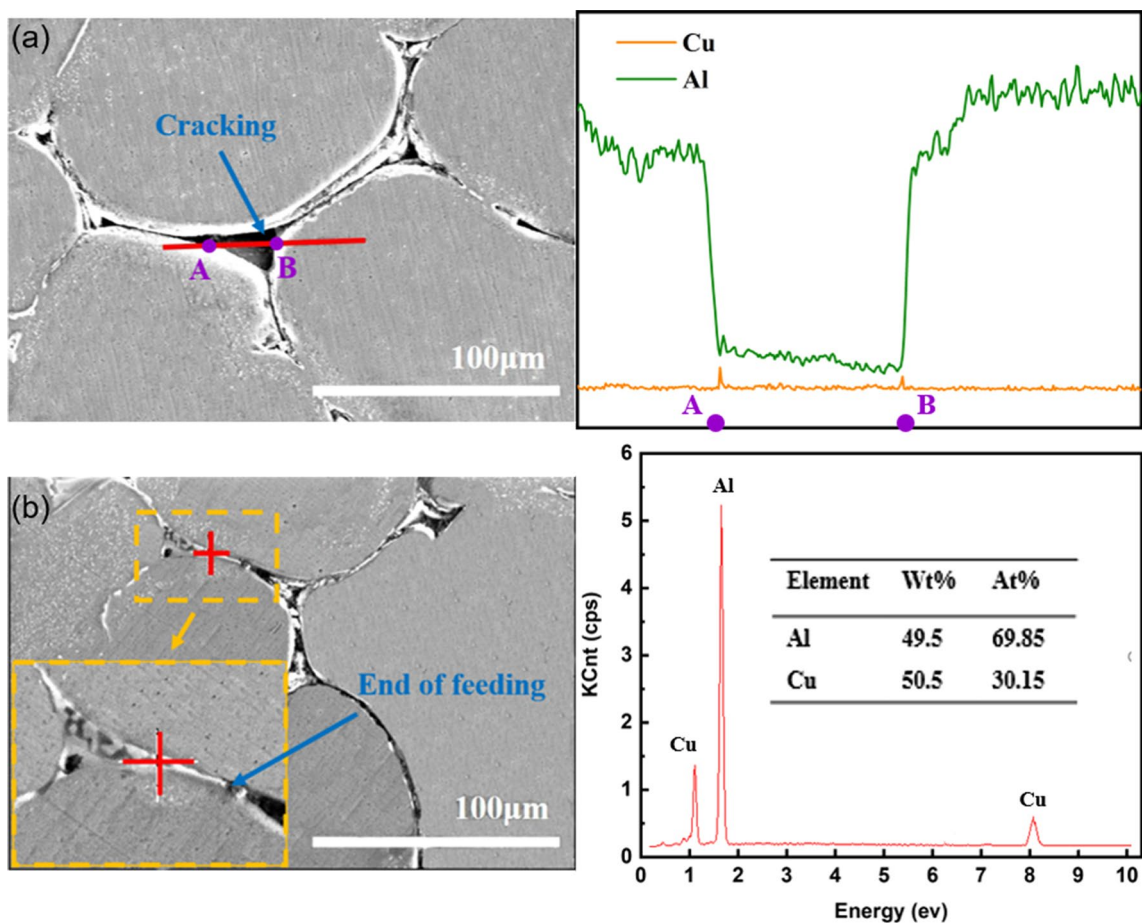
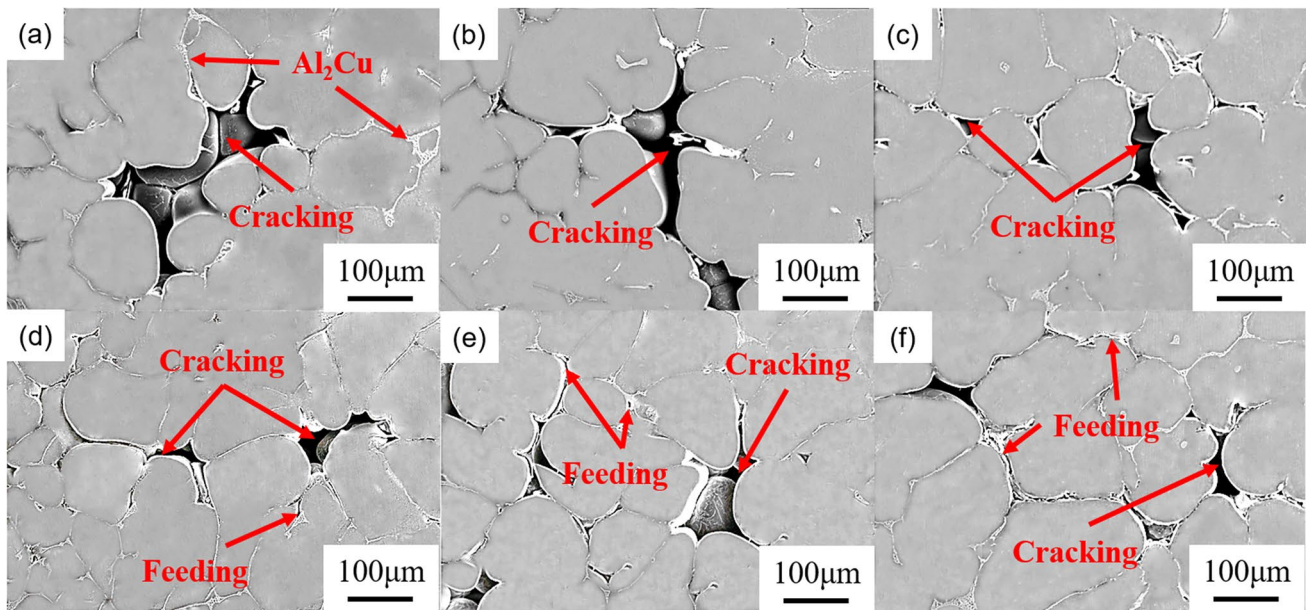**Fig. 10** Microstructures and EDS analysis of hot cracking

Fig. 11 Hot cracking morphologies after isothermal reheating treatment at 630 °C for **a** 10 min, **b** 20 min, **c** 30 min, **d** 40 min, **e** 50 min, **f** 60 min

that the thinner liquid films experienced a larger shrinkage stress at the end of solidification, and although the insufficient liquid films attempted to fill and subsequently heal the developing tears at low cooling speeds, they were not successful at completely healing the developing cracks along grain boundaries investigated in this research, which was consistent with the results of Li et al. [44] and Dou et al. [45]. As shown in Fig. 11e and f, the feeding capability was enhanced with the higher volume fraction of liquid films, which is presented later. The hot cracking morphology was similar at the three remelting temperatures.

4 Discussion

4.1 Liquid Film Characteristics Simulation

With the same isothermal remelting temperature, a longer soaking time was successful at helping Al–4Cu alloy liquid films to complete feeding by enhancing the time available for feeding and reducing the hot cracking initiation temperature, thus limiting hot cracking. This likely resulted from

the increased liquid fraction and the occurrence of Ostwald ripening. The variation in the liquid film composition was directly attributed to Ostwald ripening, which also led to different liquid film characteristics. Wang et al. [46] used Phase-Field simulations to investigate liquid channel characteristics during columnar growth of single-crystal and bicrystal Al–Cu alloys. Their results showed that a high solute content easily formed hot cracks in the liquid film at the end of solidification. Moreover, this study, with respect to the effect of liquid film characteristics on hot cracking mechanisms, creates a novel analysis with quantitative calculation through MD simulations.

Stoichiometry numbers of liquid film composition under different isothermal treatment conditions were extracted from Fig. 7b, as listed in Table 2. Based on the liquid film composition and stoichiometry numbers, atoms were randomly distributed in the $5 \times 5 \times 5$ cubic supercell with periodic boundary conditions.

RDF plays an important role in identifying the short-range order structure and atomic number of melted alloys, as reported by Xiong et al. [47]. All RDF curves showed three peaks under different isothermal remelting

Table 2 Stoichiometry numbers of liquid film composition under different isothermal treatment conditions

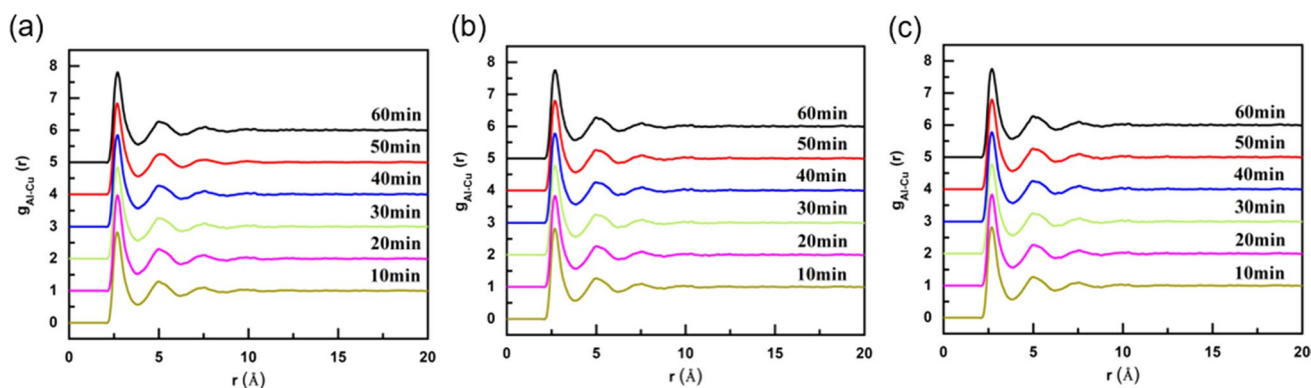| Time (min)	10	20	30	40	50	60
620	$Al_{81}Cu_{19}$	$Al_{82}Cu_{18}$	$Al_{87}Cu_{13}$	$Al_{87}Cu_{13}$	$Al_{89}Cu_{11}$	$Al_{91}Cu_9$
630	$Al_{84}Cu_{16}$	$Al_{89}Cu_{11}$	$Al_{90}Cu_{10}$	$Al_{90}Cu_{10}$	$Al_{91}Cu_9$	$Al_{93}Cu_7$
640	$Al_{88}Cu_{12}$	$Al_{89}Cu_{11}$	$Al_{90}Cu_{10}$	$Al_{90}Cu_{10}$	$Al_{95}Cu_5$	$Al_{96}Cu_4$

Fig. 12 RDFs of liquid films under different isothermal treatment conditions for **a** 620 °C, **b** 630 °C, **c** 640 °C
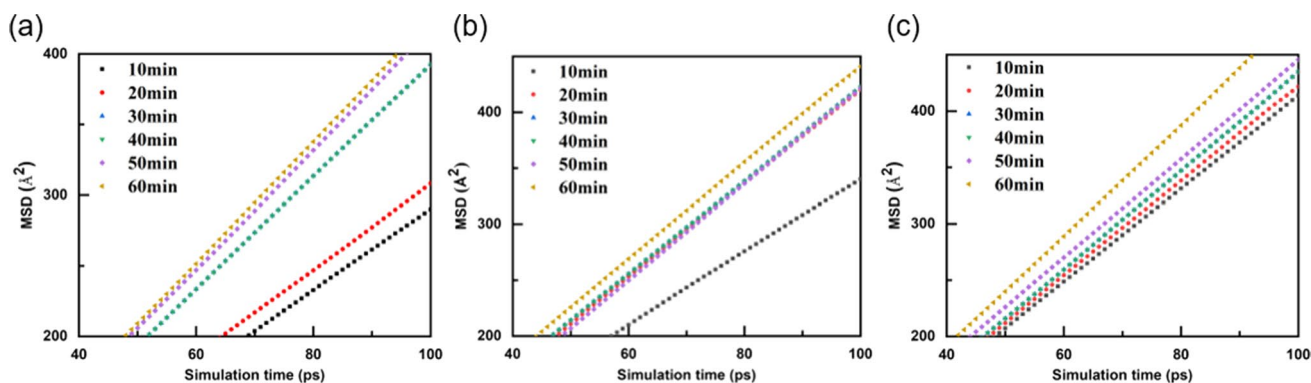

Fig. 13 MSDs of liquid films under different isothermal treatment conditions for **a** 620 °C, **b** 630 °C, **c** 640 °C

conditions, as demonstrated in Fig. 12. The same phenomenon also appeared in the study of Christian et al. [48], indicating that the liquid film exhibited a short-range order structure. The first peak value of $g(r)$ represents the radius of the effective hydrodynamic particles. The horizontal axis value ranges of the first peak were 2.67–2.69 Å, 2.69–2.71 Å and 2.69–2.71 Å corresponding to the remelting temperatures of 620 °C, 630 °C and 640 °C, respectively, while the height of every peak remained unchanged, indicating the same short-range order structure and atomic number of liquid films with different characteristics. Therefore, the difference in the feeding capability of liquid films was not related to the short-range order structure and atomic number.

Figure 13 illustrates MSD vs. soaking time curves under different isothermal remelting conditions. The linear relationship between MSDs and time implied that the established MD models enabled liquid films to reach thermal equilibrium for the selected temperature, as investigated by Wang et al. [49]. For the same temperature, the liquid film activity in thermal equilibrium increased with a longer soaking time as the MSD increment increased. This resulted from Al-rich liquid films.
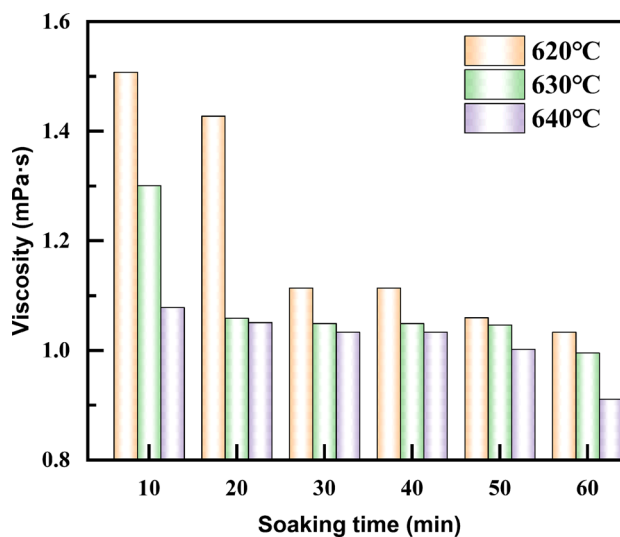

Fig. 14 Viscosities of liquid films under different isothermal treatment conditions

According to Figs. 12 and 13, the viscosities of liquid films under different remelting conditions were calculated from Eqs. (3) and (4), as depicted in Fig. 14. The viscosity of the liquid films decreased with increasing temperature and time. Section 3.2 indicates that viscosities of the liquid films were 1.51 mPa·s and 1.03 mPa·s after 10 min and 60 min soaking time for the 620 °C remelting temperature, corresponding to hot cracking initiation temperatures of 593.52 °C and 569.32 °C, respectively. However, no cracks occurred at 640 °C for 60 min, and the viscosity reached a minimum value of 0.91 mPa·s. It was concluded that the viscosity was the key property for determining the occurrence of hot cracking. Generally, higher isothermal remelting temperatures and longer soaking time were successful at enhancing the feeding capacity of liquid films by increasing the volume fraction and fluidity of liquid films but reducing their viscosity and the hot cracking initiation temperature. The results further verified the discussion in Sect. 3.2.

4.2 Hot Cracking Initiation Mechanism

According to the liquid film shrinkage stress and hot crack morphology in Sect. 3, the liquid film characteristics varied with the volume fraction and composition, as did the crystal morphology, under the same isothermal remelting temperature for different soaking time. The initiation mechanism of hot cracking in Al–4Cu alloys is presented later with respect to the effect of the crystal morphology and the volume fraction and properties of liquid films.

Previous studies have revealed that the grain refined reduces the severity of hot cracking [50–53]. A schematic diagram of the hot cracking formation mechanism is shown in Fig. 15. The liquid film was inactive in the equilibrium state; however, it had high viscosity under the same isothermal remelting temperature for a shorter soaking time. The increased feeding resistance of liquid films resulted from the coarse morphology of α-Al grains with a lower spherical degree after a shorter soaking time. The Al element melted in the liquid phase, nucleated and grew alongside α-Al grains during solidification, leading to a thinner feeding channel. Generally, the shrinkage of the liquid eutectic phase was larger than that of the solid phase at the last stage of solidification, and hot cracks were initiated by the shrinkage cavity and porosity with the presence of the solidification shrinkage force due to the insufficient feeding of liquid films, as illustrated in Fig. 15a. The same phenomenon also appeared in the studies of D 'Elia et al. [54] and Takai et al. [55], indicating that the shrinkage cavity and porosity were one of the crack sources of hot cracks. However, the thickness of the liquid film and spherical degree of grains increased, while the viscosity of the liquid films decreased after a longer soaking time. Although the feeding channels gradually narrowed during solidification, they remained larger in the alloys compared with that after a shorter soaking time. The reason for this occurrence was the lower viscosity of liquid films and the higher spherical degree of grains, as well as the wider feeding channels, after a longer soaking time. These factors facilitated the feeding behaviour, thereby inhibiting hot cracks by reducing, even eliminating, the shrinkage cavity and porosity, which is depicted in Fig. 15b. The feeding capability of liquid films peaked after 640 °C isothermal remelting temperature for 60 min,
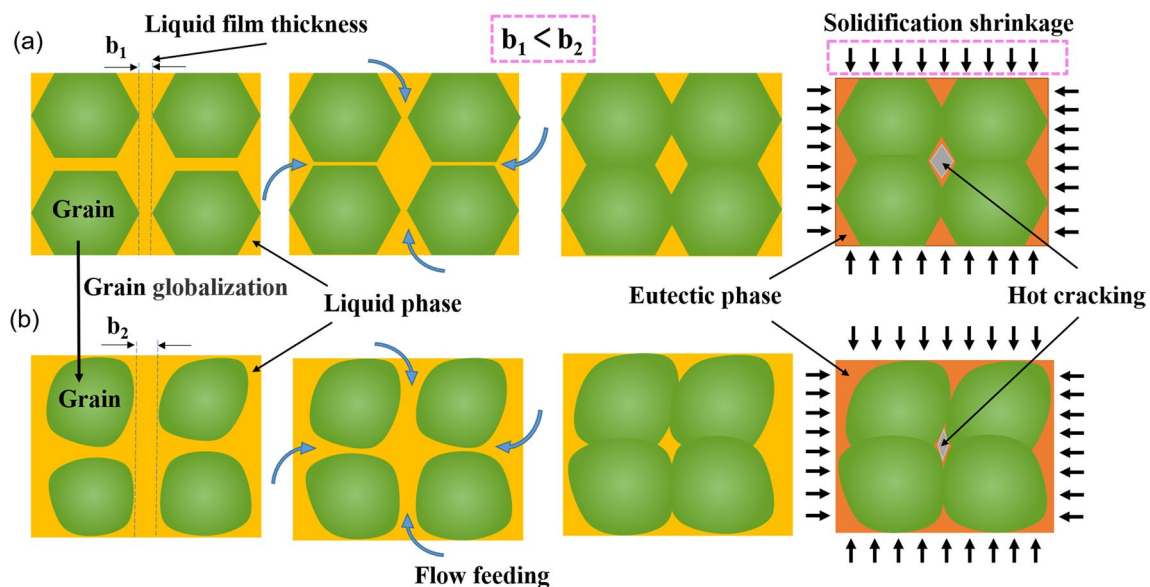

Fig. 15 Schematic diagram of the hot cracking formation mechanism **a** feeding behaviour of thin liquid film in the narrow feeding channel, **b** feeding behaviour of thick liquid film in the wide feeding channel

and almost no hot cracks were observed, while no shrinkage cavity or porosity was generated.

The liquid phase shrinkage is larger than that of the solid phase, and the theoretical shrinkage ratio of solid to liquid is 1:3 [56]. The insufficient liquid phase at the end of solidification did not effectively compensate for the shrinkage differences between the solid and liquid phases, thus inducing the shrinkage cavity and porosity. The increased hot tearing severity resulted from the induced shrinkage cavity and porosity, which became the source for developing hot cracks. The increased volume fraction associated with the wider feeding channel enhanced the time available for feeding of the liquid phase, which in turn reduced the feeding resistance. Additionally, shrinkage was likely more accommodated by the feeding of the high fluidity and excellent feeding capability of low-viscosity liquid films. Therefore, the reduction in hot cracking severity in the Al–4Cu alloy was attributed to the higher liquid fraction and grain spherical degree, as well as the lower viscosity of the liquid phase, which was beneficial for liquid films to eliminate the shrinkage difference between the solid and liquid phases.

5 Conclusions

This study systematically investigated the relationship between the liquid film volume at the end of solidification and hot cracking initiation using an MCRC apparatus. A further understanding with respect to the effect of liquid film characteristics on hot cracking initiation in Al–4Cu alloys at the end of solidification and the mechanism of hot cracking initiation was developed. The following conclusions can be drawn from this research.

1. A higher isothermal remelting temperature and longer soaking time were successful at helping Al–4Cu alloy liquid films to complete feeding during the last stage of solidification by increasing both the liquid fraction and the grain spherical degree and widening the feeding channel. A higher isothermal remelting temperature and longer soaking time reduced the hot crack initiation temperature and increased the critical crack shrinkage stress, which, in turn, limited the severity of hot tearing.
2. Molecular dynamics simulation showed that the composition of liquid films varied with isothermal remelting temperature and soaking time, while the short-range ordered structure and atomic order of liquid films remained the same. After a longer soaking time at a higher isothermal remelting temperature, the activity of the liquid film in the equilibrium state increased; however, its viscosity reduced. The increase in liquid film fluidity enhanced the filling capability.

3. The liquid fraction reached a maximum value of 36.68% at 640 °C for 60-min isothermal remelting corresponding to a valley value of liquid film viscosity of 0.91 mPa·s, and almost no hot cracks occurred under this condition.

Declarations

Conflict of interest The authors declare that they have no known competing financial interests or personal relationships that could have appeared to influence the work reported in this paper.

References

[1] S. Das, S. Das, K. Das, Compos. Sci. Technol. **67**, 746 (2007)
[2] J. Rakhmonov, K. Liu, L. Pan, F. Breton, X. GrantChen, J. Alloys Compd. **827**, 154305 (2020)
[3] S.M. Li, S. Kumar, D. Apelian, Metall. Mater. Trans. B **44**, 614 (2013)
[4] S.Y. He, C.J. Li, T.J. Zhan, W.D. Xuan, Z.M. Ren, Acta Metall. Sin. -Engl. Lett. **33**, 267 (2020)
[5] A. Barros, C. Cruz, A.P. Silva, N. Cheung, A. Garcia, O. Rocha, Acta Metall. Sin. -Engl. Lett. **32**, 695 (2019)
[6] T. Nagira, D. Yamashita, M. Kamai, H. Liu, Y. Aoki, H. Fujii, K. Uesugi, A. Takeuchi, Mater. Charact. **167**, 110469 (2020)
[7] R. Taghiabadi, A. Fayegh, A. Pakbin, M. Nazari, M.H. Ghonchen, Trans. Nonferrous Met. Soc. China **28**, 1275 (2018)
[8] F.D. Elia, C. Ravindran, Trans. Indian Inst. Met. **62**, 315 (2009)
[9] F.D. Elia, C. Ravindra, D. Sediako, Can. Metall. Q. **53**, 151 (2014)
[10] H.B. Yang, K. Zhao, J.F. Nie, X.F. Liu, Mater. Sci. Eng. A **774**, 138926 (2020)
[11] S.G. Shabestari, M.H. Ghoncheh, Metall. Mater. Trans. B **46**, 2438 (2015)
[12] J.W. Liu, S. Kou, Acta Mater. **100**, 359 (2015)
[13] J.W. Liu, S. Kou, Acta Mater. **110**, 84 (2016)
[14] D.G. Eskin, L. Katferman, Metall. Mater. Trans. A **38**, 1511 (2007)
[15] H. Ding, H.Z. Fu, Z.Y. Liu, R.Z. Chen, B.C. Liu, Z.G. Zhong, D.Z. Tang, Acta Metall. Sin. **33**, 921 (1997)
[16] Y.S. Wang, Q.D. Wang, W.J. Ding, L. Chen, Spec. Cast. Nonferrous Alloys **2**, 45 (2000)
[17] W.S. Pellini, Foundry **80**, 125 (1952)
[18] T.W. Clyne, G.J. Davies, Met. Sci. **12**, 233 (1978)
[19] R. Takai, S. Kimura, R. Kashiuchi, H. Kotaki, M. Yoshida, Mater. Sci. Eng. A **667**, 417 (2016)
[20] R. Takai, N. Endo, R. Hirohara, T. Tsunoda, M. Yoshida, Int. J. Adv. Manuf. Technol. **100**, 125 (2019)
[21] A. Matsushita, H. Mizuno, T. Okane, M. Yoshida, J. Mater. Process. Technol. **263**, 321 (2019)
[22] R.F. Xu, H.L. Zheng, J. Luo, S.P. Ding, X.L. Tian, Trans. Nonferrous Met. Soc. China **24**, 2203 (2014)
[23] R.F. Xu, H.L. Tian, Russ. J. Non-Ferrous Met. **55**, 44 (2014)
[24] Z.Y. Hou, K.J. Dong, Z.A. Tian, R.S. Liu, Z. Wang, J.G. Wang, Phys. Chem. Chem. Phys. **18**, 17461 (2016)
[25] J.G. Lee, *Computational Materials Science: An Introduction*, 2nd edn. (CRC, Boca Raton, 2016), pp.1–67

[26] O.S. Roik, O.V. Samsonnikov, V.P. Kazimirov, V.E. Sokolskii, S.M. Galushko, J. Mol. Liq. **151**, 42 (2010)

[27] W.Y. Wang, S. Shang, H.Z. Fang, H. Zhang, Y. Wang, S.N. Mathaudhu, X.D. Hui, Z.K. Liu, Metall. Mater. Trans. A **43**, 3471 (2012)

[28] Y. Zhou, P.L. Mao, L. Zhou, Z. Wang, F. Wang, Z. Liu, Mater. Lett. **271**, 127774 (2020)

[29] Y. Zhou, P.L. Mao, L. Zhou, Z. Wang, F. Wang, Z. Liu, J. Magnesium Alloys **8**, 1176 (2020)

[30] H. Atkinson, D.Y. Zhang, H.B. Dong, Metall. Mater. Trans. A **47**, 1 (2016)

[31] P.K. Seo, C.G. Kang, J. Mater. Process. Technol. **162**, 402 (2005)

[32] J.J. Wang, D. Brabazon, A.B. Phillion, G.M. Lu, Metall. Mater. Trans. A **46**, 4191 (2015)

[33] T.K. Gu, X.F. Bian, J.Y. Qin, C.Y. Xu, Phys. Rev. B **71**, 4206 (2005)

[34] Y.P. Shi, M.F. Liu, Y. Chen, X. Wang, W.L. Mo, D.Z. Li, T. Fa, B. Bai, X.L. Wang, X.Q. Chen, J. Alloys Compd. **787**, 267 (2019)

[35] J.F. Jiang, Y. Wang, H.V. Atkinson, Mater. Charact. **90**, 52 (2014)

[36] C.P. Wang, Z.J. Tang, H.S. Mei, L. Wang, R.Q. Li, Rare Met. **34**, 710 (2015)

[37] S.C. Chen, X.Q. Lin, K.Z. Zhu, Y.M. Lu, R.H. Ye, Y. Lin, X.Y. Lin, The Chin. J. Process Eng. **17**, 144 (2017)

[38] X.T. Fu, Heat Treat. **33**, 46 (2018)

[39] Y. Zhou, P.L. Mao, L. Zhou, Z. Wang, F. Wang, Z. Liu, J. Mater. Process. Technol. (2019). https://doi.org/10.1016/j.jmatprotec.2020.116679

[40] H. Hao, D.M. Maijer, M.A. Wells, A. Phillion, S.L. Cockcroft, Metall. Mater. Trans. A **41**, 2067 (2010)

[41] H.G. Zhong, X.H. Li, B. Wang, T.M. Wu, Y.H. Zhang, B. Liu, Q.J. Zhai, Met. **9**, 25 (2018)

[42] X.D. Du, F. Wang, Z. Wang, X.X. Li, Z. Liu, P.L. Mao, Acta Metall. Sin. -Engl. Lett. **33**, 1259 (2020)

[43] F.D. Elia, C. Ravindra, D. Sediako, R. Donaberger, Can. Metall. Q. **54**, 9 (2014)

[44] S. Li, D. Apelian, Int. J. Metalcast. **5**, 23 (2011)

[45] R.F. Dou, A.B. Phillion, Metall. Mater. Trans. A **47**, 4218 (2016)

[46] L. Wang, N. Wang, N. Provatas, Acta Mater. **126**, 302 (2017)

[47] L.H. Xiong, H.B. Lou, X.D. Wang, T.T. Debela, Q.P. Cao, D.X. Zhang, S.Y. Wang, C.Z. Wang, J.Z. Jiang, Acta Mater. **68**, 1 (2014)

[48] M.C. Ulrich, A. Hashibon, J. Svoboda, C. Elsässer, D. Helm, H. Riedel, Acta Mater. **59**, 7634 (2011)

[49] W.Y. Wang, J.J. Han, H.Z. Fang, J. Wang, F.Y. Liang, Acta Mater. **97**, 75 (2015)

[50] J.L. Li, R.S. Chen, Y.Q. Ma, K. Wei, Acta Metall. Sin. -Engl. Lett. **26**, 728 (2013)

[51] Y.G. Tan, F. Liu, A.W. Zhang, D.W. Han, X.Y. Yao, Acta Metall. Sin. -Engl. Lett. **32**, 120 (2019)

[52] Y. Hou, Z.Q. Zhang, W.D. Xuan, J. Wang, J.B. Yu, Z.M. Ren, Acta Metall. Sin. -Engl. Lett. **31**, 681 (2018)

[53] F. Wang, D. Ma, Z. Wang, P.L. Mao, Z. Liu, Acta Metall. Sin. **52**, 1115 (2016)

[54] F.D. Elia, C. Ravindran, D. Sediako, K.U. Kainer, N. Hort, Mater. Des. **64**, 44 (2014)

[55] R. Takai, T. Tsunoda, Y. Kawada, R. Hirohara, T. Okane, M. Yoshida, Mater. Trans. **59**, 1333 (2018)

[56] J.P. Macht, D.M. Maijer, A.B. Phillion, Mater. Trans. A **48**, 3370 (2017)